PAPER

Shock wave studies of the pyrolysis of fluorocarbon oxygenates. II. The thermal dissociation of C$_4$F$_8$O

C. J. Cobos,[a] K. Hintzer,[b] L. Sölter,[c] E. Tellbach,[c] A. Thaler[b] and J. Troe*[cd]

The thermal decomposition of octafluorooxalane, C$_4$F$_8$O, to C$_2$F$_4$ + CF$_2$ + COF$_2$ has been studied in shock waves highly diluted in Ar between 1300 and 2200 K. The primary dissociation was shown to be followed by secondary dissociation of C$_2$F$_4$ and dimerization of CF$_2$. The primary dissociation was found to be in its falloff range and falloff curves were constructed. The limiting low and high pressure rate constants were estimated and compared with modelling results. Quantum-chemical calculations identified possible reaction pathways, either leading directly to the final products of the reaction or passing through an open-chain CF$_2$CF$_2$CF$_2$ intermediate which dissociates in a second step.

1. Introduction

This article continues the series of our studies of the pyrolysis of fluorocarbon oxygenates, C$_x$F$_y$O$_z$, which was started in part I[1] with an investigation of the decomposition of perfluoroacetyl fluoride, CF$_3$COF, and of hexafluoropropene oxide, C$_3$F$_6$O. The present work describes the decomposition of the cyclic ether octafluorooxalane, C$_4$F$_8$O, which according to the present work proceeds through the pathway
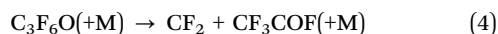
$$C_4F_8O(+M) \rightarrow CF_2 + C_2F_4 + COF_2(+M) \qquad (1)$$
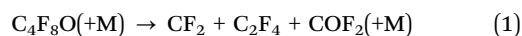
There is the possibility of the secondary dissociation of C$_2$F$_4$,

$$C_2F_4(+M) \rightarrow 2CF_2(+M) \qquad (2)$$
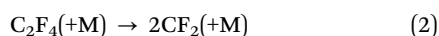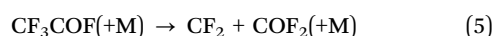
and of dimerization of CF$_2$,

$$2CF_2(+M) \rightarrow C_2F_4(+M) \qquad (3)$$
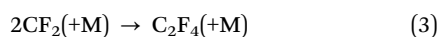
On the one hand, it is of interest to compare the primary dissociation (1) with the corresponding process for C$_3$F$_6$O,

$$C_3F_6O(+M) \rightarrow CF_2 + CF_3COF(+M) \qquad (4)$$

which is followed by

$$CF_3COF(+M) \rightarrow CF_2 + COF_2(+M) \qquad (5)$$

or

[a] *INIFTA, Facultad de Ciencias Exactas, Universidad Nacional de La Plata, Argentina*
[b] *Dyneon GmbH, Gendorf, D-84508 Burgkirchen, Germany*
[c] *Institut für Physikalische Chemie, Universität Göttingen, Tammannstrasse 6, D-37077 Göttingen, Germany. E-mail: jtroe@gwdg.de*
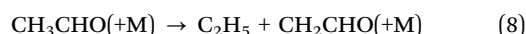[d] *Max-Planck-Institut für Biophysikalische Chemie, Am Fassberg 11, D-37077 Göttingen, Germany*

$$CF_3COF(+M) \rightarrow CF_3 + FCO(+M) \qquad (6)$$
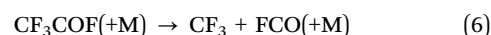
On the other hand, a comparison of the mechanism with the dissociation of tetrahydrofuran, C$_4$H$_8$O, can be made. The latter is known[2] to proceed predominantly by

$$C_4H_8O(+M) \rightarrow C_3H_6 + CH_2O(+M) \qquad (7)$$
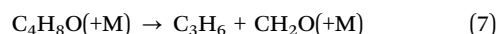
with minor contributions from

$$CH_3CHO(+M) \rightarrow C_2H_5 + CH_2CHO(+M) \qquad (8)$$

and other product channels (see ref. 2 for more details).

Like in part I,[1] the well studied[3] UV absorption of CF$_2$ proved most useful to unravel the reaction mechanism and to identify the rate and yields of primary and secondary reaction steps. On the theoretical side, quantum-chemical calculations of energy profiles and molecular parameters appeared helpful. These were followed by modelling of the rate constants, in particular in their falloff range. Without these theoretical results an analysis of the experimental results would have been difficult.

2. Experimental technique and results

The thermal decomposition of C$_4$F$_8$O was studied under high dilution by the bath gas M = Ar behind incident and reflected shock waves. The details of our experimental technique are described in part I[1] and need not to be repeated here. Analogous to our C$_3$F$_6$O-experiments, mixtures of C$_4$F$_8$O (from abcr, 97% purity) and Ar (from Air Liquide, 99.9999% purity) were prepared in large mixing vessels before the experiments. In the present case we worked with reactant concentrations between about 80 and 1030 ppm in Ar. CF$_2$ absorption signals were recorded and converted into CF$_2$-yields $Y(CF_2)$ relative to the

This journal is © the Owner Societies 2017

Phys. Chem. Chem. Phys., 2017, **19**, 3159–3164 | 3159

starting concentration $[C_4F_8O]_{t=0}$, either behind incident or reflected shock waves. This conversion was made using the temperature-dependent absorption coefficients of CF_2 at 248 nm from ref. 3.

The analysis of the experimental observations met with two complications. First, we observed marked pressure dependence of the apparent rate constants under some experimental conditions. Second, the effects of secondary reactions had to be accounted for. With respect to the latter, the following situations could be envisaged: as long as reaction (2) is much faster than reaction (1) and, at the same time, reaction (3) can be neglected, the final CF_2 yields $Y(CF_2)_{t=\infty}$ will be 3 and a first order time-law should be followed, as given by

$$[CF_2] = 3[C_4F_8O]_{t=0}\{1 - \exp(-k_1 t)\} \tag{9}$$

If reaction (2) would be slower than reaction (1), with reaction (3) still negligible, eqn (9) still would be followed, however, with the factor 3 changed to unity. As here k_2 is always much larger than k_1, this case does not apply here. The situation changes when reaction (3) comes into play. Then, the CF_2 yield will pass over a maximum before it finally decays to zero. With decreasing temperature, the maximum yields $Y(CF_2)_{max}$ also decrease. The yields then contain information on k_1, but also on the initial reactant concentration and on k_3. Under conditions where $[CF_2]$ can be considered at steady state and $k_1/k_2 \ll 1$, for $k_1 t \ll 1$ one derives

$$k_1 \approx \{Y(CF_2)_{max}\}^2 2[C_4F_8O]_{t=0} k_3 \tag{10}$$

As k_3 is a function of temperature and pressure (to be taken from ref. 1, 3, and 4), the determination of k_1 from eqn (10) is less direct than that using eqn (9). However, it allowed us to extend our experiments towards lower temperatures.

The conditions for eqn (9) are fulfilled at the higher temperatures of our experimental range. Fig. 1 illustrates CF_2 profiles which directly lead to k_1. While Fig. 1 was recorded behind a reflected shock at $T_5 = 1780$ K and $[Ar]_5 = 2.9 \times 10^{-5}$ mol cm^{-3} (leading to $k_1 = 1.6 \times 10^4$ s^{-1}), Fig. 2 shows an

Fig. 2 CF_2 yield $Y(CF_2)$ in the dissociation of C_4F_8O behind an incident shock wave ($T = 1850$ K, $[Ar] = 4.1 \times 10^{-6}$ mol cm^{-3}, $[C_4F_8O]_{t=0}/[Ar] = 1030$ ppm; time axis compressed by factor; CF_2 dissociation behind the reflected shock wave at $T = 3970$ K, $[Ar] = 9.5 \times 10^{-6}$ mol cm^{-3}, see text).

experiment where C_4F_8O decomposes behind an incident shock. At the temperature $T_2 = 1850$ K and $[Ar]_2 = 4.1 \times 10^{-6}$ mol cm^{-3}, k_1 has practically the same value as in the experiment of Fig. 1, although the temperature is higher; however, $[Ar]$ now is markedly lower. The corresponding decrease of k_1 with decreasing $[Ar]$ clearly can be attributed to falloff effects. We also note that CF_2 at the high temperature $T_5 = 3967$ K of the reflected shock in Fig. 2 decomposes with the known rate constant from ref. 5.

A low temperature experiment ($T_5 = 1306$ K) with a CF_2 maximum yield of 0.05 is illustrated in Fig. 3. One notices that the CF_2 absorption in this case shows an induction time before approaching its maximum value. It is difficult to analyse the initial rate of CF_2 formation (with $k_1 \approx 7$ s^{-1}) because of the noise of the signal. Also the incubation period, because of the contributions from reactions (1)–(3), is difficult to interpret. Therefore, here we relied on the maximum yields only which at least allowed us to extract the ratio k_1/k_3, and from this k_1.
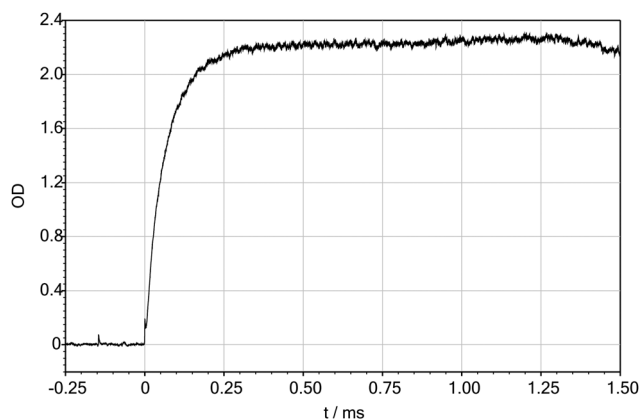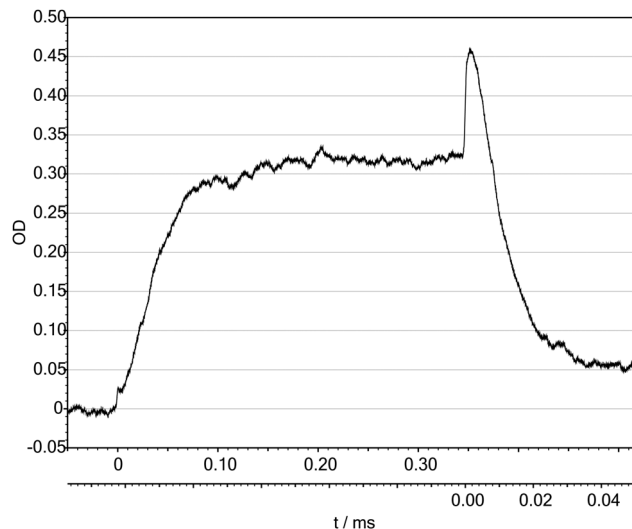

Fig. 1 CF_2 yield $Y(CF_2)$ in the dissociation of C_4F_8O behind a reflected shock wave ($T = 1780$ K, $[Ar] = 2.9 \times 10^{-5}$ mol cm^{-3}, $[C_4F_8O]_{t=0}/[Ar] = 1030$ ppm; Schlieren peaks indicate the arrival of the incident and reflected shock wave).
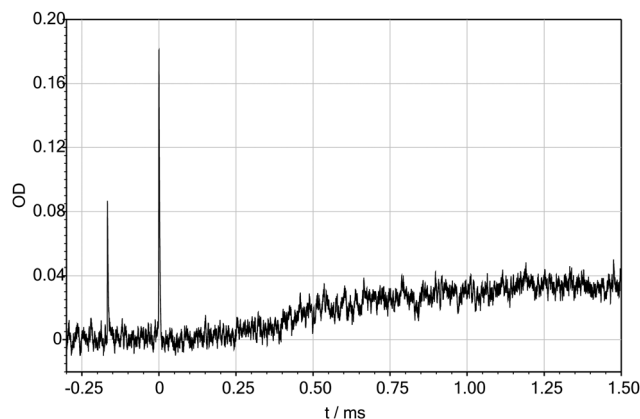

Fig. 3 As Fig. 1 ($T = 1306$ K, $[Ar] = 4.1 \times 10^{-5}$ mol cm^{-3}, $[C_4F_8O]_{t=0}/[Ar] = 545$ ppm).

3160 | Phys. Chem. Chem. Phys., 2017, 19, 3159–3164

This journal is © the Owner Societies 2017

Table 1 Rate constants k_1 for the dissociation $C_4F_8O \rightarrow CF_2 + C_2F_4 +$ COF_2 (experiments in Ar, mostly with $[C_4F_8O]_{t=0}/[Ar] \approx 1000$ ppm; upper part: results from reflected shocks, lower part: results from incident shocks; see text)

T/K	$[Ar]/10^{-5}$ mol cm^{-3}	k_1/s^{-1}
1300	4.2	7.0×10^0
1342	4.1	2.7×10^0
1364	4.1	1.2×10^1
1410	3.9	2.5×10^1
1453	3.8	6.1×10^1
1599	3.2	1.5×10^3
1644	3.3	2.3×10^3
1689	3.1	4.5×10^3
1750	2.9	9.8×10^3
1779	2.9	1.6×10^4
1836	2.7	3.3×10^4
1927	2.5	7.0×10^4
2019	2.3	1.5×10^5
2178	2.2	2.4×10^5
1742	0.46	9.2×10^3
1850	0.41	2.0×10^4
2003	0.37	4.8×10^4
2210	0.30	7.8×10^4
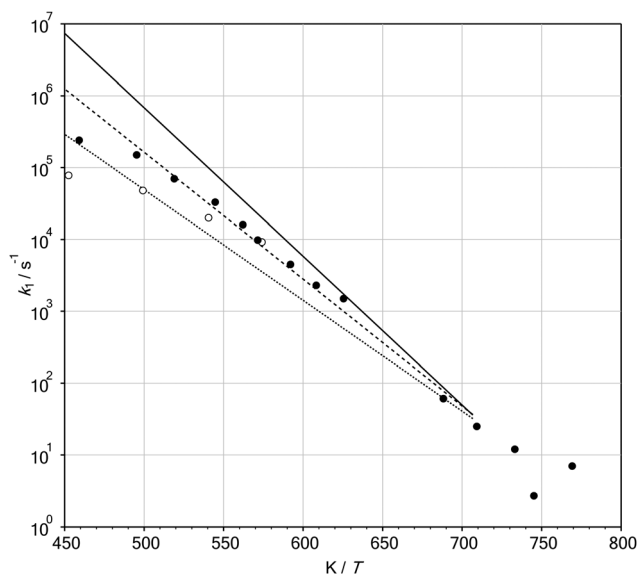
Fig. 4 Rate constants k_1 for C_4F_8O dissociation (1) ($\bigcirc$: $[Ar] = (3-5) \times 10^{-6}$ mol cm^{-3}; $\bullet$: $[Ar] = (2-5) \times 10^{-5}$ mol cm^{-3}; lines from bottom to top: Arrhenius representations with eqn (12) for $\bigcirc$, with eqn (11) for $\bullet$, and with eqn (13) for $k_{1,\infty}$).

Table 1 summarizes rate constants and experimental conditions. Fig. 4 provides an Arrhenius representation of k_1 for groups of higher and lower bath gas concentrations [Ar]. These results are later compared with modelled falloff curves. The "raw data" summarized in Table 1 and in Fig. 4 should be commented. The data above about 1600 K are all from experiments in which the reaction could be monitored until $Y(CF2) \approx 3$ was attained. In this case, the rate law of eqn (9) could be used for the determination of k_1. The data below about 1500 K were all from experiments where this procedure was not applicable. Here, the maximum yields $Y(CF_2)_{max}$ were below about 0.05 and eqn (10)

was exploited, leading to k_1 on the basis of the known values[1,4] of k_3. We also did experiments in the intermediate range 1500–1600 K, but here the evaluation depended on the accurate knowledge of k_2 and k_3 in a too sensitive way to allow for a sufficiently accurate determination of k_1. However, the CF_2-signals over the accessible observation time (≤ 1.5 ms) in this range within the uncertainties were consistent with the mechanism of reactions (1)–(3).

The numerical representation of the data from Table 1 and Fig. 4 is done best by taking into account the modelling results given below. These indicate that only little falloff of k_1 is expected for the present experiments at $T \leq 1500$ K, whereas marked falloff of k_1 should be expected at $T \geq 2000$ K. This conclusion is reached independent of modelling uncertainties (see below). We, therefore, represent the data by two expressions, one for $[Ar] \approx (2-5) \times 10^{-5}$ mol cm^{-3} and one for $[Ar] \approx (3-5) \times 10^{-6}$ mol cm^{-3}. As the latter data were only accessible in the high-temperature groups of experiments, in accordance with the modelling we assume that below 1500 K all low-pressure data of our experiments nearly coincide with the high-pressure data. In this way two Arrhenius expressions are obtained:

$$k_1 \approx 1.1 \times 10^{14} \exp(-338 \text{ kJ mol}^{-1}/RT) \text{ s}^{-1} \quad (11)$$

for $[Ar] \approx (2-5) \times 10^{-5}$ mol cm^{-3} and

$$k_1 \approx 2.5 \times 10^{12} \exp(-295 \text{ kJ mol}^{-1}/RT) \text{ s}^{-1} \quad (12)$$

for $[Ar] \approx (3-5) \times 10^{-6}$ mol cm^{-3}. Fig. 4 includes these representations of k_1.

3. Quantum-chemical calculations and rate constant modelling

The present quantum-chemical calculations, like in part I,[1] were performed at the G4MP2 *ab initio* composite level[6] using the Gaussian 09 software.[7] The G4MP2 model used B3LYP/6-31G(2df,p) optimized geometries and harmonic vibrational frequencies scaled by the factor 0.9854. The influence of the basis set on the derived quantities was studied in additional calculations with the larger basis set B3LYP/6-311+G(3df) (unscaled), leading to results denoted by G4MP2//B3LYP/6-311+G(3df) (abbreviated as G4MP2* in the following). The dissociation pathways were explored such as illustrated by their transition state structures TS1 and TS2 in Fig. 5 which also includes the parent molecule C_4F_8O. Fig. 6 illustrates the structures of the $(CF_2)_3$ intermediate of the pathway TS2 and TS3 on the way to $C_2F_4 + CF_2$. Fig. 7 shows the energetics of the two pathways with the transition state structures TS1 and TS2 (and TS3). The calculated molecular parameters of the parent molecule and the transition states are summarized in the Appendix. On the basis of the determined molecular parameters, we then modelled dissociation rate constants. We took into account that falloff effects of the rate constants had to be expected. For this reason, we calculated limiting high pressure rate constants $k_{1,\infty}$ by ordinary rigid activated complex transition state theory, limiting low pressure rate constants $k_{1,0}$ following the
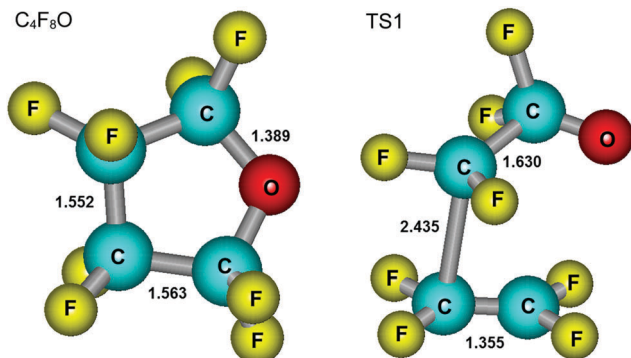
This journal is © the Owner Societies 2017

Phys. Chem. Chem. Phys., 2017, **19**, 3159–3164 | **3161**

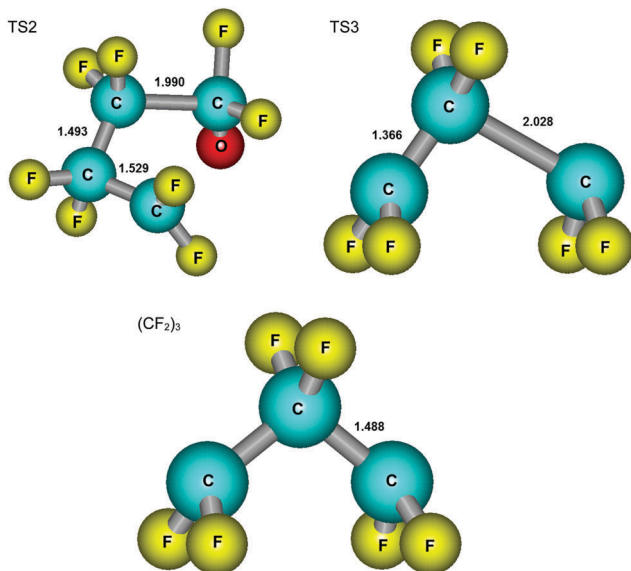Fig. 5 Structures of C_4F_8O and TS1 from G4MP2* calculations (see text, bond lengths in Å).
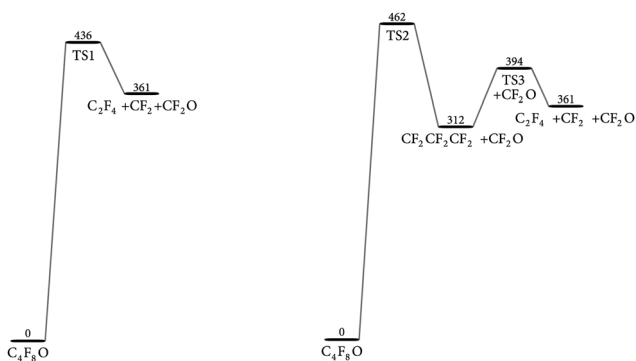

Fig. 6 As Fig. 5, for TS2, TS3, and $(CF_2)_3$.

Fig. 7 Energy profiles (at 0 K, in kJ mol^{-1}) for the TS1 pathway (left) and TS2 pathway (right).

method outlined in ref. 8 and we estimated center broadening factors $F_{cent,1}$ following ref. 8 and 9. Full falloff curves were represented by the method described in ref. 10 (see below).

Table 2 Modelled high pressure rate constants $k_{1,\infty}$ (in s^{-1}, for 1500 and 2000 K; calculations for G4MP2* models with torsions, one free rotor (Rot$_1$), or three free rotors (Rot$_{1,2,3}$) and for transition states TS1 and TS2, see text and Appendix)

Model	$k_{1,\infty}$ (1500, TS1)	$k_{1,\infty}$ (1500, TS2)	$k_{1,\infty}$ (2000, TS1)	$k_{1,\infty}$ (2000, TS2)
Torsion	1.6×10^1	1.3×10^{-1}	1.3×10^5	1.9×10^3
Torsion + Rot$_1$	6.8×10^1	7.6×10^{-1}	5.0×10^5	9.2×10^3
Torsion + Rot$_{1,2,3}$	1.2×10^4	3.9×10^2	3.9×10^7	3.7×10^6

The reaction enthalpy (at 0 K) for $C_4F_8O \rightarrow C_2F_4 + CF_2 + CF_2O$ was determined to be 362.8 kJ mol^{-1} at the G4MP2 level and 361.1 kJ mol^{-1} at the G4MP2* level. The corresponding transition state enthalpies were 433.9 (G4MP2) and 435.6 (G4MP2*) kJ mol^{-1} for TS1, and 461.5 (G4MP2) and 461.9 (G3MP2*) kJ mol^{-1} for TS2. The estimation of $k_{1,\infty}$ is complicated by the presence of three low-frequency torsional modes in both TS1 and TS2, whose hindered rotational barriers were not determined. We, therefore, alternatively treated the torsion by harmonic oscillators or by free rotors. These operations markedly affected the calculated values of $k_{1,\infty}$. Interestingly, the two pathways responded in quite different ways to the transition from torsions to free rotations. Table 2 illustrates this by modelled values of $k_{1,\infty}$ for 1500 and 2000 K. In view of the great variation of the modelled $k_{1,\infty}$ in Table 2, it appeared unavoidable to determine $k_{1,\infty}$ from the experiments. This, however, required falloff corrections. Fortunately, these corrections did not depend too much on the chosen $k_{1,\infty}$. However, a distinction between the pathways TS1 and TS2 was not possible.

In order to construct full falloff curves, also limiting low pressure rate constants had to be estimated. As this is usually the case, the average energy $\langle \Delta E \rangle$ transferred by collision had to be left as a fitting parameter. In the present case, we explored values of $-\langle \Delta E \rangle / hc = 50$, 100, and 200 cm^{-1}. Finally, center broadening factors were estimated with the methods of ref. 9–11. The resulting values are given in the Appendix. Choosing the representation of reduced falloff curves $k_1/k_{1,\infty}$ as a function of $k_{1,0}/k_{1,\infty}$ (with $k_{1,0} \propto$ [Ar]) from ref. 10 and 11 (also given in the Appendix), one obtains falloff curves such as illustrated in Fig. 8. Here the torsional model for the TS1 pathway is chosen for illustration. Indeed, one observes only very minor falloff corrections at 1500 K for [Ar] = 5×10^{-5} mol cm^{-3}. On the other hand, measurements at 2000 K and [Ar] = 5×10^{-5} mol cm^{-3} should lead to k_1 which is about a factor of 5 below $k_{1,\infty}$. In addition, k_1 should increase by about a factor of 2–3 when [Ar] is increased from 4×10^{-6} to 2×10^{-5} mol cm^{-3}. Obviously these estimates can only be semi-quantitative, but we note that they correspond to all models considered and are consistent with our experimental observations. More qualitative details are included in the Appendix. Neglecting falloff corrections to the measured k_1 at 1500 K and applying a falloff correction of about a factor of 5 to the measured k_1 at 2000 K and [Ar] = 2×10^{-5} mol cm^{-3}, we derive $k_{1,\infty}$ in the form

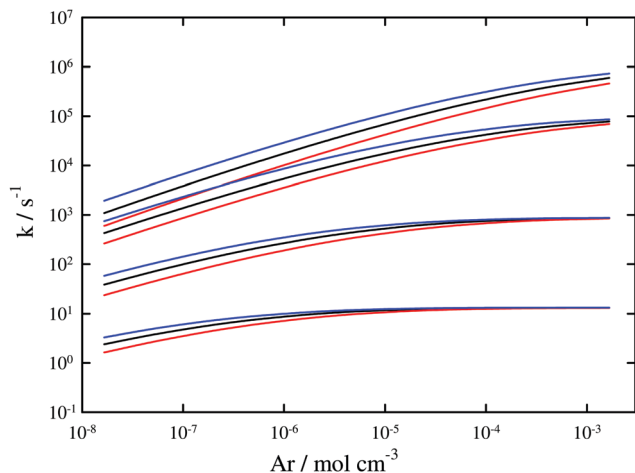$$k_{1,\infty} \approx 1.5 \times 10^{16} \exp(-396 \text{ kJ mol}^{-1}/RT) \text{ s}^{-1} \quad (13)$$

3162 | Phys. Chem. Chem. Phys., 2017, 19, 3159–3164

This journal is © the Owner Societies 2017

Fig. 8 Falloff curves for k_1 with the TS1 torsion model (see Appendix 3 and 4; calculations for 1500, 1700, 2000, and 2200 K from bottom to top; $-\langle \Delta E \rangle /hc$ in cm^{-1}: 50 for red curves, 100 for black curves, and 200 for blue curves).

Comparing the corresponding values for 1500 and 2000 K of 2.5×10^2 and 7×10^5 s^{-1}, resp., with the values from Table 2, we conclude that a pure torsional model underestimates the experimental results. Instead some rotor distributions must be included in $k_{1,\infty}$. We repeat that unfortunately we cannot distinguish between the TS1 and TS2 pathways.

4. Discussion

Breaking the ring structure and releasing CF_2 requires much more energy in C_4F_8O than in C_3F_6O. The lower temperatures required for the decomposition of C_3F_6O are responsible for the fact that this reaction (at the pressures of the present shock wave experiments) is close to the first order high pressure limit of the unimolecular dissociation. In studying the decomposition of C_4F_8O at considerably larger temperatures, the dissociation shows marked falloff effects, i.e. is of intermediate reaction order between (1) and (2).

The two pathways for C_4F_8O decomposition illustrated in Fig. 7, with a single barrier TS1 or two barriers TS2 and TS3 and a $(CF_2)_3$ intermediate, are sufficiently close in energy that minor entropic differences (torsions or rotors) may favour one or the other. The present experiments did not allow for a distinction between the two pathways. However, in any case the high pressure rate constant $k_{1,\infty}$ was found to have a large preexponential factor near 10^{16} s^{-1} such as this is normal for simple bond scissions (see e.g. ref. 1 for C_2F_4 dissociation). It appears worth noticing that the primary dissociation (7) of tetrahydrofuran has a rate constant[2] of $k_{7,\infty} \approx 3 \times 10^{16} \exp(347 \text{ kJ mol}^{-1}/RT)$ s^{-1} which is not too much different from $k_{1,\infty}$ from eqn (13) and also falls into the class of simple bond scissions. The present work again illustrates the value of complementary experimental and modelling approaches to kinetic problems of the described kind. Nevertheless, due to the large number of relevant and not well known molecular parameters, only a semi-quantitative interpretation of the experimental data can be presently achieved.

Appendix

1. Molecular parameters for C_4F_8O dissociation (calculations at the G4MP2//B3LYP/6-311+G(3df) level, see text)

Energies (at 0 K, in kJ mol^{-1})

C_4F_8O: 0; TS1: 435.6; TS2: 461.9; $(CF_2)_3$ + COF_2: 311.7; TS3: 393.7; C_2F_4 + CF_2 + COF_2: 361.1.

Vibrational frequencies (in cm^{-1})

C_4F_8O: 43, 60, 193, 227, 244, 262, 302, 304, 324, 352, 367, 410, 417, 536, 557, 592, 601, 644, 662, 705, 810, 965, 1023, 1076, 1164, 1184, 1188, 1194, 1231, 1243, 1307, 1319, 1382

TS1: 146i, 29, 59, 97, 114, 137, 158, 178, 188, 215, 221, 273, 281, 387, 401, 489, 547, 553, 558, 577, 618, 666, 747, 805, 811, 899, 1201, 1293, 1321, 1368, 1422, 1658, 1768

TS2: 383i, 46, 68, 126, 147, 167, 186, 209, 217, 271, 277, 304, 349, 392, 421, 504, 540, 556, 568, 596, 629, 699, 766, 835, 987, 1023, 1044, 1185, 1210, 1358, 1432, 1499, 1721

Rotational constants (in cm^{-1})

C_4F_8O: 0.0360, 0.0276, 0.0238; σ = 2.

TS1: 0.0345, 0.0235, 0.0203; σ = 1.

TS2: 0.0344, 0.0262, 0.0222; σ = 1.

2. Modelling of high pressure rate constants $k_{1,\infty}$

TS1, torsion model: $k_{1,\infty} \approx 4.0 \times 10^{16} \exp(-444 \text{ kJ mol}^{-1}/RT)$ s^{-1} torsion + free rotor models (ν in cm^{-1}, I_{red} in amu Å^2)

(a) TS1 torsion CF_2CF_2–CF_2COF_2: ν = 29, I_{red} = 128;

(b) TS1 torsion $CF_2CF_2CF_2$–COF_2: ν = 97, I_{red} = 76;

(c) TS1 torsion CF_2–$CF_2CF_2COF_2$: ν = 221, I_{red} = 39;

(d) TS2 torsion CF_2CF_2–CF_2COF_2: ν = 209, I_{red} = 126;

(e) TS2 torsion $CF_2CF_2CF_2$–COF_2: ν = 167, I_{red} = 76;

(f) TS2 torsion CF_2–$CF_2CF_2COF_2$: ν = 68, I_{red} = 42;

T = 1500 K: $k_{1,\infty}$ (a)/$k_{1,\infty}$ = 4.3, $k_{1,\infty}$ (b)/$k_{1,\infty}$ = 10.8, $k_{1,\infty}$ (c)/$k_{1,\infty}$ = 16.6; $k_{1,\infty}$ (d)/$k_{1,\infty}$ = 28.4, $k_{1,\infty}$ (e)/$k_{1,\infty}$ = 18.0, $k_{1,\infty}$ (f)/$k_{1,\infty}$ = 5.7

3. Modelling of low pressure rate constants $k_{1,0}$/[Ar] and center broadening factors F_{cent} (for the torsion model and $-\langle \Delta E \rangle /hc$ = 100 cm^{-1})

$k_{1,0} \approx 8.2 \times 10^{24}(T/2000 \text{ K})^{-28.5} \exp(-482 \text{ kJ mol}^{-1}/RT)$ cm^3 mol^{-1} s^{-1}, F_{cent} = 0.010, 0.012, 0.018, 0.022 for T = 1500, 1700, 2000, and 2200 K, resp. (black curve in Fig. 8).

4. Representation of falloff curves (from ref. 10 and 11):

$k_1/k_{1,\infty} = [x/(1+x)]F_{cent}(x)$ with $x = k_{1,0}/k_{1,\infty}$ and $F_{cent}(x) = (1+x)/(1+x^n)^{1/n}$, where $n = [\ln 2/\ln(2/F_{cent}(x))][0.8 + 0.2x^q]$ and $q = [F_{cent}(x) - 1]/\ln[F_{cent}(x)/10]$.

References

1 C. J. Cobos, K. Hintzer, L. Soelter, E. Tellbach, A. Thaler and J. Troe, *Phys. Chem. Chem. Phys.*, 2016, DOI: 10.1039/C6CP06816B.

2 M. Verdicchio, B. Sirjean, L. S. Tran, P.-A. Glaude and F. Battin-Leclerc, *Proc. Combust. Inst.*, 2015, **35**, 533–541.

3 C. J. Cobos, A. E. Croce, K. Luther, L. Soelter, E. Tellbach and J. Troe, *J. Phys. Chem. A*, 2013, **117**, 11420–11429.

4 C. J. Cobos, L. Sölter, E. Tellbach and J. Troe, *J. Phys. Chem. A*, 2014, **118**, 4873–4879.

5 C. J. Cobos, A. E. Croce, K. Luther and J. Troe, *J. Phys. Chem. A*, 2010, **114**, 4755–4761.

6 L. A. Curtiss, P. C. Redfern and K. Raghavachari, *J. Chem. Phys.*, 2007, **127**, 124105.

7 M. J. Frisch, *et al.*, *Gaussian 09, Revision A.02–SMP*, Gaussian, Inc., Wallingford, CT, 2009.

8 J. Troe, *J. Phys. Chem.*, 1979, **83**, 114–126.

9 J. Troe, *Ber. Bunsenges. Phys. Chem.*, 1983, **87**, 161–169.

10 J. Troe and V. G. Ushakov, *Z. Phys. Chem.*, 2014, **1**, 1–10.

11 J. Troe and V. G. Ushakov, *J. Phys. Chem.*, 2011, **135**, 054304.